A Variable-DC-Offset Modulation Scheme for Improved Performance of a Differential-Mode Inverter

Kartik Tank, Shantanu Gupta, *Graduate Student Member, IEEE*, Man Mohan Garg, *Senior Member, IEEE*, Sudip K. Mazumder, *Fellow, IEEE*, and Moien Mohamadi, *Student Member, IEEE*

***Abstract*—In this article, a novel continuous modulation scheme with variable-dc-offset (CMS-VDO) is proposed for a single-phase differential-mode inverter (DMI). The output voltage of the DMI is the difference in output voltages of two differentially connected dc–dc converters. CMS-VDO is so designed that the output voltage of the individual dc/dc converter is reduced without affecting the output voltage of the DMI. This reduced voltage yields reductions in circulating current, peak switch voltage, total harmonic distortion, and improved efficiency compared to conventional modulation scheme with fixed dc offset (CMS-FDO). The experimental results compare and validate the improved inverter performance using CMS-VDO over CMS-FDO.**

***Index Terms*—Differential mode, efficiency, harmonic distortion, inverter, modulation, switch stress.**

I. Introduction

SINGLE phase inverters are widely used to convert the dc electrical energy to an ac electrical energy compatible with household and industrial appliances. Furthermore, inverters are also widely used to harvest the renewable [e.g., photovoltaic (PV)] energy [1], [2], [3] and support battery energy storage [4], where such energy sources have varying dc output voltage. Performance of an inverter is generally measured by its capability to efficiently generate a low-total harmonic distortion (THD) ac sinusoid. Widely used implementation of inverters are generally realized using full-bridge voltage-source inverters (VSIs) which are buck dc/ac converters [5]. The VSIs typically require four switches per phase, and the dc-source voltage should always be higher than the peak of the output ac voltage. The dc-voltage constraint of the buck converter is addressed by adding another dc/dc converter stage. For low-power inverter implementation, the two-stage inverter solution results in a higher component count, complex control, and lower overall efficiency [5].

Single-stage inverter solutions with a wide dc swing necessitates buck–boost capability. A z-source dc/ac converter [6] is a single-stage solution and typically needs two active switches. However, the input and output currents of inverter are discontinuous and require additional filter circuit. Quasi-z-source inverter [7], [8] allows continuous input and output current; however, the average- and ripple-current stresses on the inductor and the switches are significant resulting in a reduced inverter efficiency.

A differential-mode converter [9], [10], [11] consists ideally of two identical dc/dc converter modules. In a differential-mode inverter (DMI [9]), the two modules are connected in parallel at the dc side while at the ac side, the modules are differentially connected. The two modules are operated to generate a bipolar (i.e., an ac) output voltage. Such DMIs, based on buck, boost, and buck–boost converters, are discussed in [10]. The Ćuk-based implementation of such a DMI, referred in this article as a differential-mode Ćuk inverter (DMCI) has step-up/-down and continuous input- and output-current capabilities [9]. As shown in Fig. 1, the DMCI topology requires four active switches and eight passive components. The input and output inductors of the dc/dc modules can be integrated to reduce the magnetic component counts [12], [13], [14], [15]. In addition, the DMCI also allows isolation feature as presented in [9], [15], [16], and [17].

In [16], [18], [19], and [20], a conventional continuous modulation scheme with fixed dc offset (CMS-FDO) for the DMI is discussed which governs the operation of the two dc/dc modules. The continuous operation of the dc/dc modules in CMS-FDO results in a lower THD as the even harmonics generated by non-linearities in the modules get largely cancelled [16]. However, the CMS-FDO-based DMI suffers from higher circulating power resulting in reduced efficiency and higher peak switch voltages due to the higher dc-offset voltage of the individual dc/dc converter module.

In [16], a discontinuous modulation scheme (DMS) for an isolated DMI is outlined which results in higher inverter efficiency due to reduced circulating power and also lower switch voltage stress compared to that obtained using CMS-FDO. As the two modules are not operating continuously, the THD of the DMS-based open-loop DMI is higher and requires a close-loop control mechanism to limit the THD below 5%.

Manuscript received 15 May 2023; revised 10 August 2023; accepted 18 September 2023. Date of publication 27 September 2023; date of current version 23 October 2023. This work was supported in part by NSF under Award 2052316. Recommended for publication by Associate Editor C. N. M. Ho. *(Kartik Tank, Shantanu Gupta, Man Mohan Garg, and Sudip K. Mazumder contributed equally to this work.) (Corresponding author: Sudip K. Mazumder.)*

Kartik Tank and Man Mohan Garg are with the Department of Electrical Engineering, Malaviya National Institute of Technology Jaipur, Jaipur 302017, India (e-mail: 2020ppd5492@mnit.ac.in; mmgarg.ee@mnit.ac.in).

Shantanu Gupta, Sudip K. Mazumder, and Moien Mohamadi are with the Department of Electrical and Computer Engineering, University of Illinois Chicago, Chicago, IL 60607 USA (e-mail: sgupt57@uic.edu; mazumder@uic.edu; mmoham65@uic.edu).

Color versions of one or more figures in this article are available at https://doi.org/10.1109/TPEL.2023.3319589.

Digital Object Identifier 10.1109/TPEL.2023.3319589

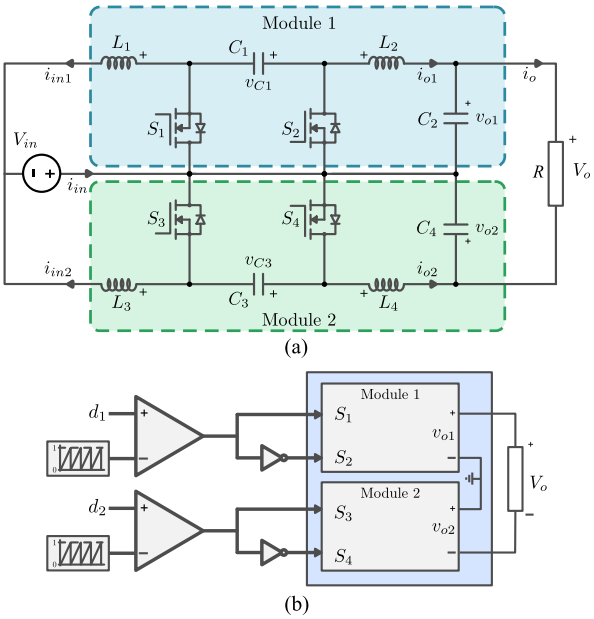

Fig. 1. (a) Illustration of a DMCI with two DC–DC converter modules. (b) Modulation mechanism of the DMCI.

In [21], a novel continuous modulation scheme with variable-dc-offset modulation scheme (CMS-VDO) for DMI is outlined by the authors. CMS-VDO modulation for buck-, boost-, and buck–boost-derived DMI is discussed. A variable-dc voltage offset for both the dc/dc modules output is used to overcome the drawbacks of CMS-FDO yielding lower circulating power and lower switch voltage stress. Cáceres and Barbi [10] presents simulation results to validate the operation of CMS-VDO. A comparison of CMS-FDO and CMS-VDO is also presented.

Unlike [21], in this article, detailed analyses of DMCI's circulating power and switch voltage stress are conducted for CMS-VDO to understand the dependencies of these parameters with varying DMCI operating conditions. Furthermore, detailed experimental evaluations of the CMS-VDO- and CMS-FDO-based DMCI are also presented to support the analyses. Additionally, THD, efficiency, and unity- and non-unity-power-factor-load performances of the DMCI using the two modulation schemes are also demonstrated.

Overall, in Section II, an outline on CMS-FDO and CMS-VDO is provided. In Section III, comparison between CMS-FDO and CMS-VDO regarding voltage stress and circulating current is carried out. Section IV provides detailed experimental results associated with the two modulation schemes for the DMCI. Finally, Section V captures the conclusions.

II. Modulation Schemes for DMCI

The single-phase DMCI topology is shown in Fig. 1(a). DMCI consists of ideally two identical dc/dc Ćuk modules (Modules 1 and 2) connected in parallel at the dc side of the inverter while the outputs of the two modules are connected differentially at the ac side. The modulation mechanisms of the two dc/dc converter modules are shown in Fig. 1(b).

As shown in the figure, the duty cycle, d_1 is applied to Module 1 while the duty cycle, d_2 is applied to Module 2. Switch S_1 of Module 1 is operated using pulsewidth modulation (PWM) associated with d_1 while S_2 is operated complementarily with the duty cycle $d'_1 = 1 - d_1$. Similarly, switching of S_3 in Module 2 is governed by PWM based on the duty cycle d_2 while S_4 is switched complementarily based on the duty cycle, $d'_2 = 1 - d_2$. As both the modules are supplied with the input voltage, V_{in}, the output voltages of the two modules in terms of respective duty cycles of the modules are the same as of Ćuk dc/dc converter [22] and given by the following expressions:

$$v_{o1} = \frac{d_1}{1-d_1} V_{\text{in}} \tag{1a}$$

$$v_{o2} = \frac{d_2}{1-d_2} V_{\text{in}}. \tag{1b}$$

The ac output voltage (v_o) of the DMCI is the voltage difference between the output voltages (v_{o1} and v_{o2}) of Modules 1 and 2 and is given by

$$v_o = v_{o1} - v_{o2} = \left(\frac{d_1}{1-d_1} - \frac{d_2}{1-d_2}\right) V_{\text{in}}. \tag{2}$$

Equation (2) demonstrates that the modulation scheme for the DMCI dictates the output of individual dc/dc converter modules to generate the desired sinusoid ac output voltage. The description of the CMS-VDO and CMS-FDO is discussed in the following section.

A. CMS-FDO

In CMS-FDO, the two dc/dc converter modules of the DMCI are so operated that $d_1 + d_2 = 1$ [9]. Applying this duty-cycle relationship of CMS-FDO and using (2), the following relation for the inverter output voltage is obtained:

$$v_o = V_m \sin(\omega t) = \left(\frac{d_1}{1-d_1} - \frac{1-d_1}{d_1}\right) V_{\text{in}} \tag{3}$$

where V_m is the required peak of the desired output ac (sinusoidal) voltage and ω is the angular frequency of the output voltage. Solving the quadratic equation in (3), d_1 (and hence $d_2 = 1 - d_1$) is found to be

$$d_1 = 0.5 + \frac{\sqrt{4 + (g\sin(\omega t))^2} - 2}{2g\sin(\omega t)} \tag{4a}$$

$$d_2 = 0.5 - \frac{\sqrt{4 + (g\sin(\omega t))^2} - 2}{2g\sin(\omega t)} \tag{4b}$$

where g is defined by V_m/V_{in}. Following (4), Fig. 2 captures the variation in d_1 and d_2 for CMS-FDO.

Voltages, v_{o1} and v_{o1} are obtained using (1) and (4):

$$v_{o1} = \left(\frac{g\sin(\omega t)}{2} + \sqrt{1 + \left(\frac{g\sin(\omega t)}{2}\right)^2}\right) V_{\text{in}} \tag{5a}$$

$$v_{o2} = \left(-\frac{g\sin(\omega t)}{2} + \sqrt{1 + \left(\frac{g\sin(\omega t)}{2}\right)^2}\right) V_{\text{in}}. \tag{5b}$$

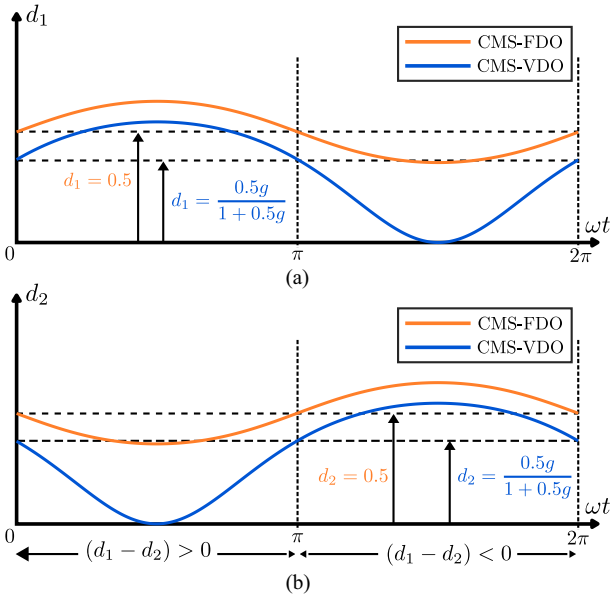

Fig. 2. Variation in (a) d_1 and (b) d_2 for CMS-FDO and CMS-VDO modulated DMCI over a line cycle.

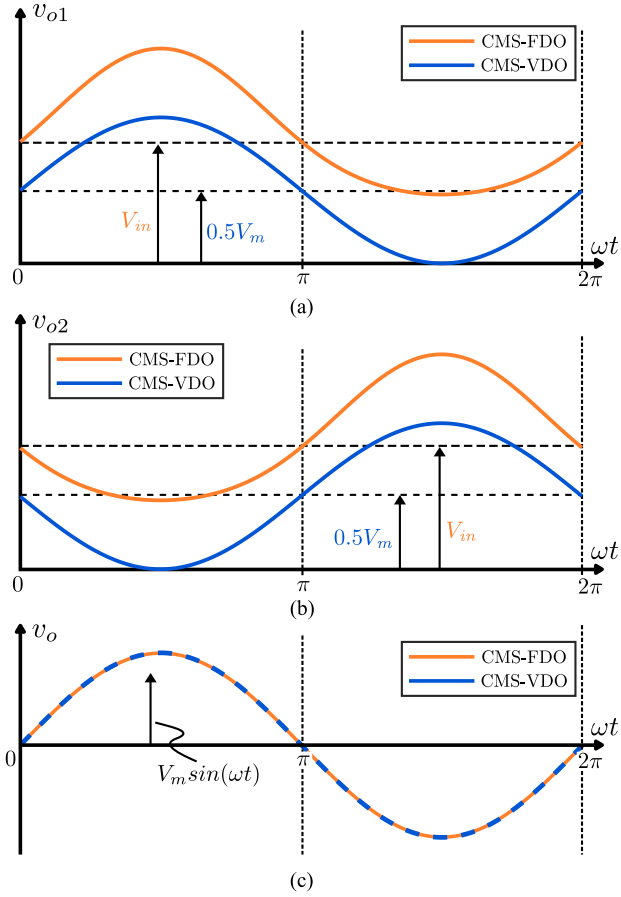

Fig. 3. Output voltages of (a) module 1, (b) module 2, and (c) the DMCI over a line cycle operated using CMD-FDO and CMS-VDO.

The output voltages of Modules 1 and 2 are shown in Fig. 3(a) and (b), respectively, using the duty-cycle variation shown in Fig. 2. Fig. 3(c) shows the desired sinusoidal output voltage, v_o, which is obtained by taking the difference of the output voltages of the two dc/dc converter modules. For the CMS-FDO, the fixed dc bias of 0.5 in the duty cycles results in an offset of V_{in} on the output of the dc/dc converter modules regardless of the normalized gain g.

In CMS-FDO, the module dc-offset voltage is not varied instead, it is set at V_{in}, which generally yields higher module output voltage. The reduction in the dc-offset voltage at the output of each module leads to a reduction in the circulating power and switch voltage stress as detailed in Section III.

B. CMS-VDO

In the CMS-VDO, d_1 and d_2 are so determined that the inequality $V_{\text{in}} - 0.5V_m \geq 0$. In addition, because the output voltage of the inverter is determined by the differences in the output voltages of the two dc/dc converter modules, the minimum output voltages of the modules also contribute more to building the desired inverter output voltage. The CMS-VDO has been proposed considering these aspects. In a CMS-VDO-based DMCI, each dc/dc converter module produces a sinusoidal output voltage with dc-offset volage $= 0.5gV_{\text{in}}$ yielding the following:

$$v_{o1} = (0.5g + 0.5g\sin(\omega t))\ V_{\text{in}} \tag{6a}$$

$$v_{o2} = (0.5g - 0.5g\sin(\omega t))\ V_{\text{in}}. \tag{6b}$$

It is evident that $0.5V_m$ is not fixed but a function of the peak output voltage. For instance, when the voltage of the second module is at its minimum, the first module needs to generate less voltage (compared to that needed for CMS-FDO) to have the same inverter output voltage. Duty cycles d_1 and d_2 are obtained using (1) and (6) and are given by the following equations:

$$d_1 = \frac{0.5g + 0.5g\sin(\omega t)}{1 + 0.5g + 0.5g\sin(\omega t)} \tag{7a}$$

$$d_2 = \frac{0.5g - 0.5g\sin(\omega t)}{1 + 0.5g - 0.5g\sin(\omega t)}. \tag{7b}$$

Fig. 2 shows the duty cycles for CMS-VDO (along with that for CMS-FDO) of the two dc/dc converter modules for the same inverter output voltage. Fig. 3 shows the module voltages and inverter output voltage for the CMS-VDO along with the CMS-FDO obtained using the duty cycles shown in Fig. 2.

Fig. 4(a) and (b) show the variation in the desired DMCI output voltage (i.e., $V_m\sin(\omega t)$) normalized to the input voltage (i.e., V_{in}) with varying duty cycle d_1 for CMS-FDO and CMS-VDO $g = 1.2$. Fig. 4(a) shows that, for CMS-FDO, even though the normalized dc/dc converter module output voltages are nonlinear functions of the duty cycle, the inverter normalized output voltage appears almost a linear function of the duty cycle. Fig. 4(b) shows that, for CMS-VDO, the inverter and module normalized output voltages are nonlinearly related to the duty cycle. As the minimum gain of the individual module is zero, the gain trace of the modules shifts with varying g. Finally, for the

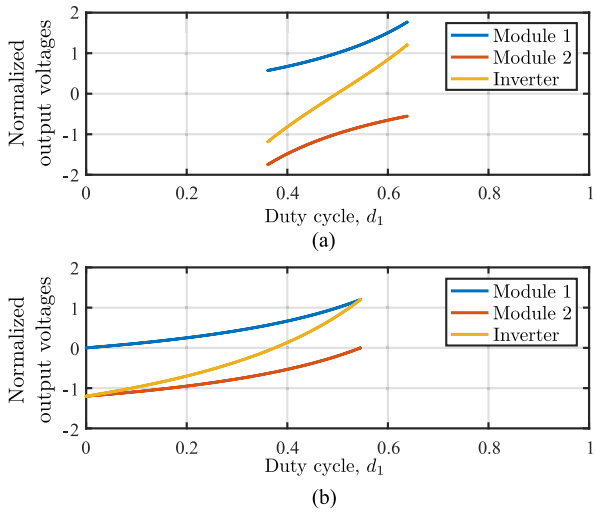

Fig. 4. Inverter and module output voltages (normalized to the input voltage) with varying duty cycle for (a) CMS-FDO and (b) CMS-VDO.

same, normalized inverter output voltage, CMS-FDO normalized module output voltages are found to be higher indicating a higher switch voltage stress.

III. Comparison of CMS-VDO and CMS-FDO

In this section, a comparative analysis of CMS-VDO and CMS-FDO is provided to outline the advantage of CMS-VDO. The following analysis assumes an ideal DMCI where the switches and the passive components are assumed to be ideal.

A. Switch Voltage Stress

The peak voltage across the switches in a Ćuk derived converter is dictated by the peak voltage across the blocking capacitor (e.g., C_1 in Module 1). The voltage across the blocking capacitor is the sum of the instantaneous input and output voltages of the Ćuk module. Hence, the peak voltage stress across the switches for Module 1 is given by the following:

$$V_{\text{peak}} = v_{o1,\text{peak}} + V_{\text{in}}. \tag{8}$$

Using (5), (6), and (8), peak voltage stress for CMS-FDO and CMS-VDO are given by (9) and (10), respectively:

$$V_{\text{peak,CMS-FDO}} = V_{\text{in}} \left(1 + \frac{g}{2} + \sqrt{1 + \left(\frac{g}{2}\right)^2}\right) \tag{9}$$

$$V_{\text{peak,CMS-VDO}} = V_{\text{in}} \left(1 + g\right). \tag{10}$$

Fig. 5 illustrates the peak switch voltage for the two modulation schemes for varying g. It indicates that, the peak switch voltage stress increases with an increase in the magnitude of the output voltage of the DMCI for both CMS-FDO and CMS-VDO. However, the peak switch voltage stress is significantly higher for CMS-FDO compared to CMS-VDO, especially for lower g.

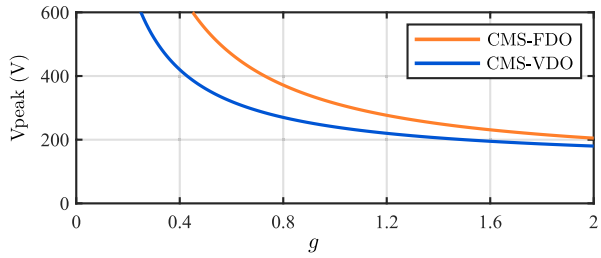

Fig. 5. Peak switch voltage as a function of g for $V_m = 120$ V.

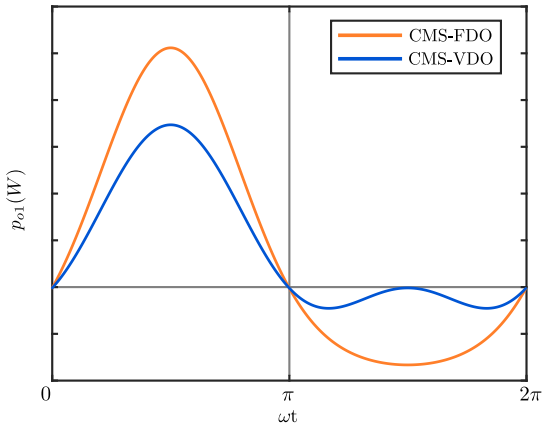

Fig. 6. Instantaneous output power of a DMCI module over a line cycle for CMS-FDO and CMS-VDO.

B. Circulating Power

As the two dc/dc converter modules of the DMCI operate in an identical manner except for the out-of-phase operation, analysis of only the first module is provided. Due to a cascaded connection of the modules at the output side, the load current is also the output current of each of the two modules. Hence, the instantaneous output power of the DMCI module, $p_{o1}(t)$, is given by the following:

$$p_{o1} = v_{o1}\, i_o \tag{11}$$

where $i_o\,(t) = i_{o1}\,(t) = -i_{o2}(t)$ ignoring the switching ripple. Using (5), (6), and (11), the instantaneous output power for CMS-FDO and CMS-VDO for a unity-power-factor load are determined to be the following:

$$p_{o1,\text{CMS-FDO}} = \frac{V_{\text{in}}^2}{R}\, g_s \left(\frac{g_s}{2} + \sqrt{1 + \left(\frac{g_s}{2}\right)^2}\right) \tag{12}$$

$$p_{o1,\text{CMS-VDO}} = \frac{V_{\text{in}}^2}{R}\, g_s \frac{(g + g_s)}{2} \tag{13}$$

where $g_s = g\sin(\omega t)$ and R is the resistive load.

Using (12) and (13), and for the same input and output voltages, the instantaneous power of the DMCI module operating with CMS-FDO and CMS-VDO are plotted in Fig. 6 for $g = 1.2$. Fig. 6 implies that, even though the output power of the inverter is the same (given the same output voltage and resistive load) for both the modulation schemes, the individual module

of the inverter handles more power when it is operated using CMS-FDO rather than CMS-VDO. This indicates the presence of higher circulating power for CMS-FDO-based DMCI.

The circulating power reflects the additional power, beyond the power that needs to be delivered to the load, which circulates in a dc/dc converter module of the DMCI [2]. As such, such a circulating power is not desired in a DMCI since it results in additional dc/dc converter module (and hence inverter) losses. Additionally, a lower circulating power also yields reduced current and/or voltage stress for the same power delivered to the load.

In this article, the ratio of the circulating (reactive) power to the active power for the DMCI module is used to assess the extent of the circulating power. The reactive power (Q_{o1}) through a DMCI module can be derived from apparent power, S_{o1}, and active power, P_{o1}, over a line cycle period, T, as captured by the following relationship:

$$S_{o1}^2 = P_{o1}^2 + Q_{o1}^2 = V_{o1}^2\, I_o^2 \tag{14}$$

where

$$V_{o1}^2 = \frac{1}{T}\int_0^T v_{o1}^2 dt$$

$$I_o^2 = \int_0^T i_{o1}^2 dt.$$

V_{o1} and I_o represent the root-mean-square (RMS) values of v_{o1} and i_{o1}, respectively. The ratio of the reactive power to the active power is given by the following:

$$\frac{Q_{o1}}{P_{o1}} = \sqrt{\frac{\frac{1}{T}\int_0^T v_{o1}^2 dt \frac{1}{T}\int_0^T i_o^2 dt}{\left[\frac{1}{T}\int_0^T v_{o1} i_o dt\right]^2} - 1}. \tag{15}$$

Using (5), (6), and (12), the ratio of Q_{o1}/P_{o1} for the CMS-FDO and CMS-VDO operated DMCI is determined to be the following:

$$\left(\frac{Q_{o1}}{P_{o1}}\right)_{\text{CMS-FDO}} = \sqrt{\frac{g^2+8}{g^2}} \tag{16a}$$

$$\left(\frac{Q_{o1}}{P_{o1}}\right)_{\text{CMS-VDO}} = \sqrt{\frac{\frac{1}{T}\int_0^T \left(0.5V_m\left(1+\sin(\omega t)\right)\right)^2 dt \frac{1}{T}\int_0^T \left(\frac{V_m}{R}\sin(\omega t)\right)^2 dt}{\left[\frac{1}{T}\int_0^T \frac{V_m^2}{2R}\left(1+\sin(\omega t)\right)\sin(\omega t)\, dt\right]^2} - 1}$$

$$\left(\frac{Q_{o1}}{P_{o1}}\right)_{\text{CMS-VDO}} = \sqrt{2} \tag{16b}$$

which indicates that unlike the CMS-FDO, the ratio of reactive to active power in CMS-VDO is independent of g.

Fig. 7 shows the comparison of the ratio of the reactive (circulating) power to the active power for varying g. It shows that, the reactive (circulating) power for the CMS-FDO-based DMCI is significantly higher than that obtained using CMS-VDO-based DMCI at lower g. With increasing g, this difference between the two modulation schemes narrows.

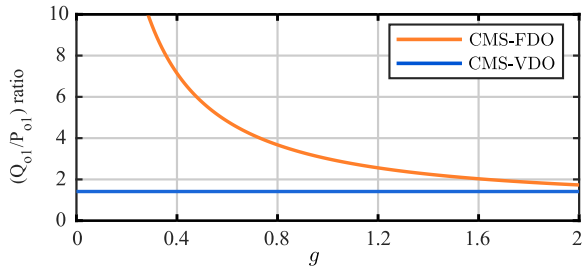

Fig. 7. Ratio of reactive (circulating) to active power for varying peak-normalized DC-voltage gain (g).

C. Current Stress

The current through the switches in a Ćuk derived converter is sum of the instantaneous input and output current of the Ćuk module. As the modules are assumed to be identical, the current stress on both the modules are equal, hence, only Module 1 is used to analyze the current stress. For an ideal Ćuk module, the peak current through the switches over a switching period is given by the following:

$$I_{\text{sw}} = \langle I_{\text{sw}} \rangle + \Delta I_{\text{sw}}. \tag{17a}$$

In (17a), I_{sw} is the average current through the switches over a switching period and is given by the following equation:

$$\langle I_{\text{sw}} \rangle = \left(v_{o1}/V_{\text{in}} + 1\right) i_{o1} \tag{17b}$$

and ΔI_{sw} is the ripple current through the switches. By using volt-second balance on the input and output inductor currents, ΔI_{sw} is given by the following:

$$\Delta\, I_{\text{sw}} = \frac{V_{\text{in}} d_1}{2 f_{\text{sw}}}\left(\frac{1}{L_1} + \frac{1}{L_2}\right). \tag{17c}$$

where L_1 and L_2 is the input and output inductors, respectively. From (17c), ΔI_{sw} for Ćuk module is proportional to the duty cycle of the module which is shown in Fig. 2 for a constant V_{in}. Using (5)–(7), the average current through the switches for the CMS-FDO and CMS-VDO operated DMCI is determined to be the following:

$$\langle I_{\text{sw}} \rangle_{\text{CMS-FDO}} = \left(\frac{g_s}{2} + \sqrt{1 + \left(\frac{g_s}{2}\right)^2} + 1\right)\left(\frac{g_s V_{\text{in}}}{R}\right) \tag{18}$$

$$\langle I_{\text{sw}} \rangle_{\text{CMS-VDO}} = (0.5g + 0.5g_s + 1)\left(\frac{g_s V_{\text{in}}}{R}\right). \tag{19}$$

The peak value of ripple current through the switches for the CMS-FDO and CMS-VDO operated DMCI occurs at the peak of output voltage and is obtained by substituting (4) and (7) into (17c). The peak value of the current ripple through the switch is given by the following:

$$\Delta I_{\text{sw,pk,CMS-FDO}} = \frac{V_{\text{in}}}{2 f_{\text{sw}}}\left(0.5 + \frac{\sqrt{4+g^2}-2}{2g}\right)\left(\frac{1}{L_1} + \frac{1}{L_2}\right) \tag{20}$$

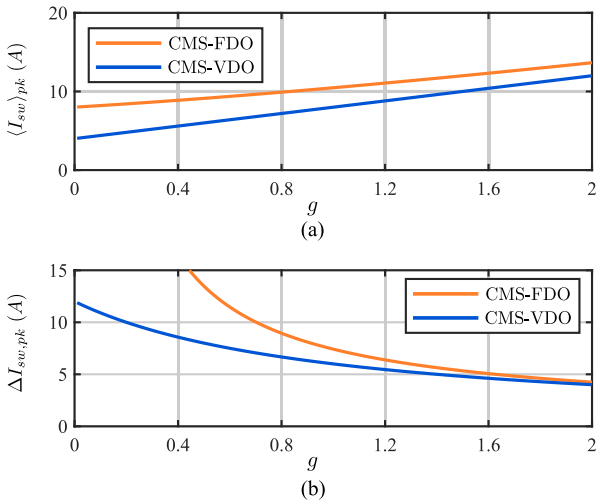

Fig. 8. (a) Peak value of average current, and (b) peak value of ripple current through the switches for varying peak-normalized DC-voltage gain (g) with $V_m = 120$ V and $R = 30\ \Omega$.

$$\Delta\, I_{\mathrm{sw,pk,CMS-VDO}} = \frac{gV_{\mathrm{in}}}{2f_{\mathrm{sw}}}\left(\frac{1}{1+g}\right)\left(\frac{1}{L_1}+\frac{1}{L_2}\right). \tag{21}$$

Fig. 8(a) shows the comparison of the peak value of the average current through the switches for CMS-FDO and CMS-VDO operated DMCI using (18) and (19). As shown in Fig. 8(a), the peak value of the average current through the switches is found to be higher using CMS-FDO compared to CMS-VDO, which results in a higher conduction loss.

In Fig. 8(b), the peak value of ripple current through the switches is shown for CMS-FDO and CMS-VDO operated DMCI. The peak value of ripple across the switches is higher for CMS-FDO compared to CMS-VDO. The difference is significantly higher for lower g due to higher duty cycle (higher module voltage) in case of CMS-FDO compared to CMS-VDO. The high ripple at lower g results in higher conduction losses in the switch.

As the switch current is the sum of the input and output inductor currents, the higher switch current also indicates higher current through the inductors which increases magnetic conduction losses. The ripple current through an inductor produces varying magnetic flux field in the magnetic core. Higher ripple current in the case of CMS-FDO compared to CMS-VDO causes higher nonlinear magnetic core losses [12], [23] especially for lower g.

IV. Experimental Results

An experimental prototype of the DMCI is developed to validate the analysis regarding CMS-VDO and provide comparison with CMS-FDO. Fig. 9 shows a hardware prototype of the DMCI with the specifications provided in Table I. A TMS320F28335 digital signal processor based controller manufactured by Texas Instruments is used to generate the desired PWM signals for the CMS-VDO- and CMS-FDO-based DMCI. A PA3000 power analyzer manufactured by Tektronix is used to measure the efficiency, and the output-voltage THD of the inverter. The same

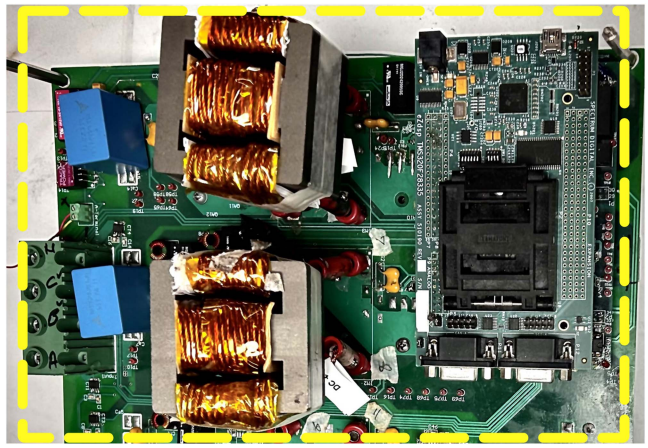

Fig. 9. Experimental prototype of the DMCI.

TABLE I
Parameters of the Experimental DMCI Prototype

Input voltage, V_{in}	70 – 150 Vdc
Gain, g	0.8 – 1.7
Output frequency, f	50–60 Hz
Full load resistance, R	30 Ω
DC side filter inductance L_1, L_3	145 µH
AC side filter inductance L_2, L_4	161 µH
Blocking capacitance C_1, C_3	1.5 µF
AC side capacitance C_2, C_4	3.3 µF
Switching frequency, f_{sw}	50 kHz

hardware prototype is used for both CMS-FDO and CMS-VDO-operated DMCI for experimental comparison and validation.

The inverter waveform for a unity-power-factor load of 30 Ω and $g = 1.2$ is shown in Fig. 10. Fig. 10(a) shows the waveform for CMS-FDO-based DMCI. The modulation scheme is realized using the duty cycle relation given by (4) for the desired output voltage. As outlined earlier and illustrated in Fig. 3, the output voltages of the dc/dc converter modules of the DMCI have a dc offset equaling the input voltage. The difference of the output voltages of the modules results in the sinusoidal output voltage of the DMCI.

Fig. 10(b) shows waveforms for the CMS-VDO modulated DMCI; the modulation scheme is realized following (7). The minimum value of the output voltage of a DMCI module operated with CMS-VDO is 0 V, which results in a lower circulating current. The peak output voltage of a DMCI module operated with CMS-FDO is found to be 179 V while the peak output voltage of a DMCI module operated with CMS-VDO is found to be 122 V for the same inverter RMS output voltage (V_o) of 85 V. The higher module output voltage for the CMS-FDO-based DMCI results in a higher switch-voltage stress.

In Fig. 11, the waveforms for the DMCI operated with a load of power factor 0.9 are shown to demonstrate the abilities of the CMS-VDO and CMS-FDO to support active as well as reactive power. Equations (4) and (7) show that for the ideal DMCI, operated, respectively, using CMS-FDO and CMS-VDO, the duty cycles are not dependent on the load current or the load

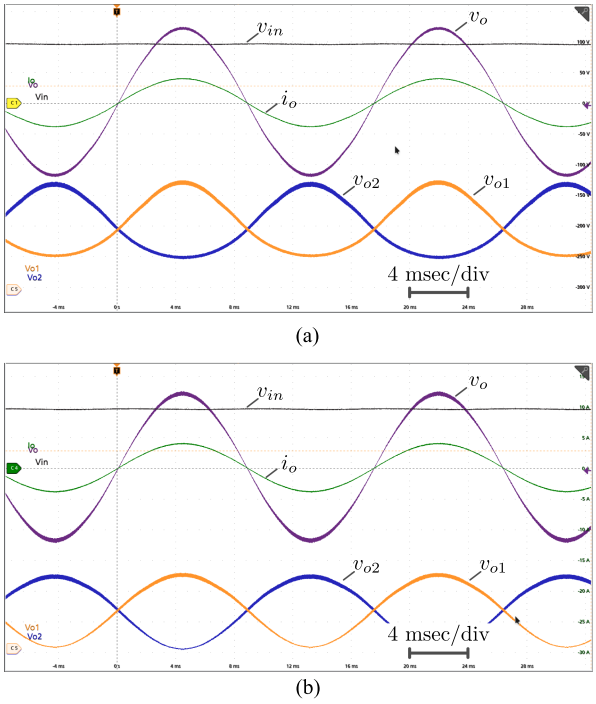

Fig. 10. Experimental waveforms of the DMCI with (a) CMS-FDO, and (b) CMS-VDO at $R = 30\ \Omega$ and $g = 1.2$. The output voltage of the DMCI is the purple trace (50 V/div), the output current is the green trace (5 A/div), the output voltage of module 1 is the orange trace (50 V/div), and the output voltage of module 2 is the blue trace (100 V/div). The time scale is 4 msec/div.

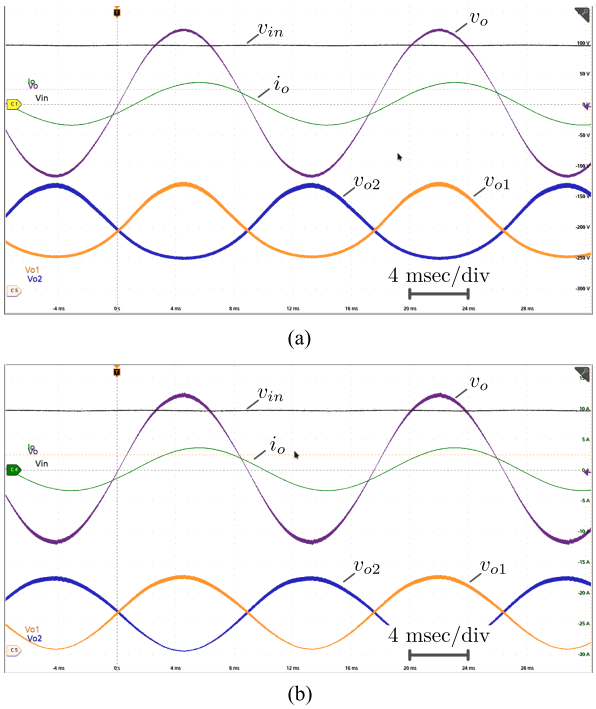

Fig. 11. Experimental waveforms of the DMCI with (a) CMS-FDO, and (b) CMS-VDO at $R = 30\ \Omega$, $L = 40$ mH, and $g = 1.2$. The output voltage of DMCI is the purple trace (50 V/div), the output current is the green trace (5 A/div), the output voltage of module 1 is the orange trace (50 V/div), and the output voltage of module 2 is the blue trace (100 V/div). The time scale is 4 msec/div.

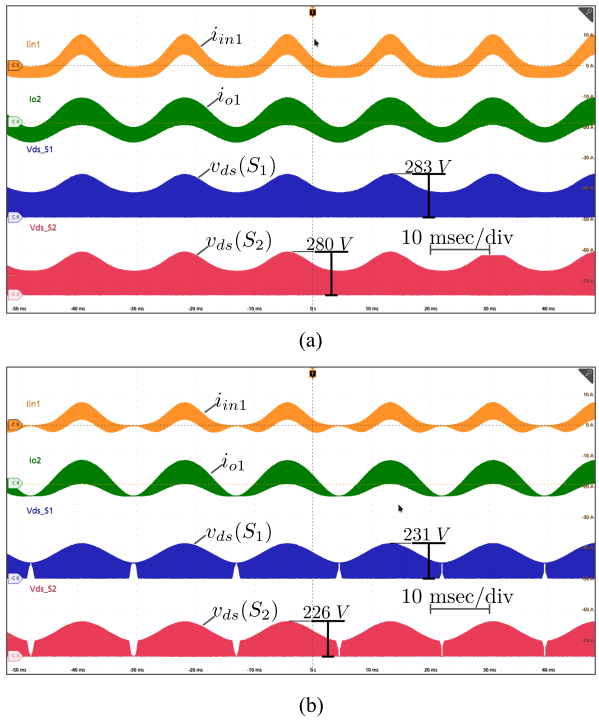

Fig. 12. Input and output currents and switch voltages for one of the modules (module 1) of the DMCI, which is operated using (a) CMS-FDO and (b) CMS-VDO. The load resistance (R) is set at 30 Ω while g is set at 1.2. The orange trace is the input inductor current (10 A/div), the green trace is the output inductor current (10 A/div), the blue trace is the drain-to-source voltage of S_1 (200 V/div), and the red trace is the drain-to-source voltage of S_2 (200 V/div). The time resolution for the horizontal axis is set at 10 msec/div.

power factor. As such, (4) and (7) are also used to operate the DMCI for the nonunity-power-factor load with a resistance of 30 Ω and an inductance of 40 mH. The results for both the modulation schemes are obtained for $g = 1.2$ and the same RMS output voltage of 85 V.

Fig. 12 shows the waveforms of Module 1 while the DMCI is operated with CMS-FDO and CMS-VDO and feeds a load of 30 Ω with $g = 1.2$. The figure shows that the peak of the input inductor current for the CMS-FDO-based DMCI is higher than that obtained using the CMS-VDO-based DMCI. Since the input voltage for both the modulation schemes are kept the same, a higher input current for the CMS-FDO-based DMCI implies that the inverter for this case draws a higher circulating (reactive) power.

Furthermore, the RMS input (output) inductor current for the CMS-FDO- and CMS-VDO-operated DMCI, following Fig. 12, are found to be 3.5 A (3.5 A) and 2.2 A (3.2 A), respectively. The higher current ripples of the inductors for the CMS-FDO-based DMCI results in higher copper and core magnetic losses.

Fig. 12 also shows that the peak switch voltages for a CMS-FDO-based DMCI module are about 21% higher compared to that obtained using CMS-VDO-based DMCI. This is because the switch voltage, which is nominally dictated by the blocking capacitor voltage (that in turn, is the sum of the input and output voltages of a module), is higher for the CMS-FDO-based DMCI given its higher output voltage. The higher voltages across the

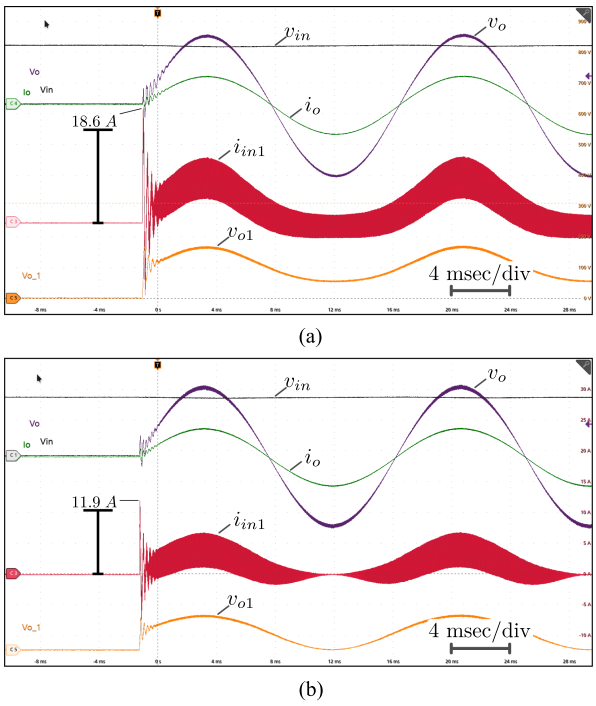

Fig. 13. Transient response of the DMCI using (a) CMS-FDO and (b) CMS-VDO. The load resistance (R) is set at 60 Ω while g is set at 1.2. The input voltage of DMCI is the black trace (50 V/div), the output voltage of DMCI is the purple trace (50 V/div), the green trace is the output current (2 A/div), the red trace is the input inductor current (5 A/div), and the output voltage of Module 1 is the orange trace (100 V/div). The time resolution for the horizontal axis is set at 4 msec/div.

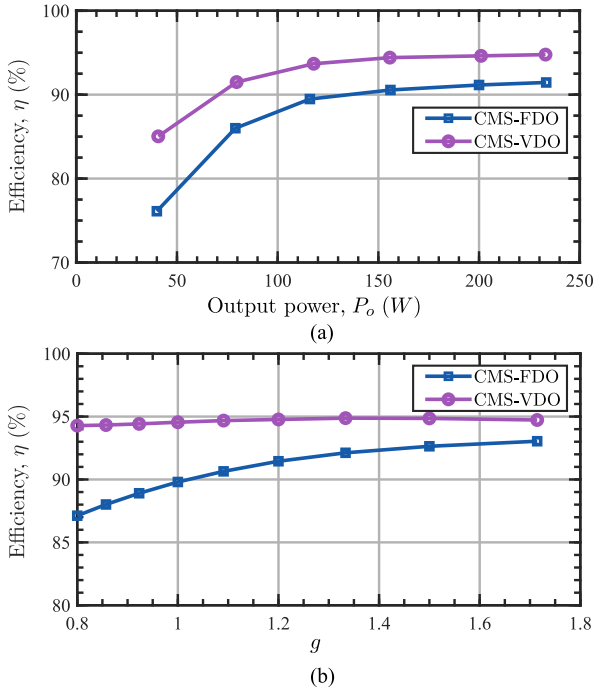

Fig. 14. Comparison of efficiencies of CMS-FDO, and CMS-VDO-based DMCI operated with constant $V_o = 85$ VRMS for varying (a) output power and (b) normalized gain.

switches coupled with higher current ripples (alluded to in the earlier paragraph) also yield higher losses for the switches of the CMS-FDO-based DMCI.

In Fig. 13, dynamic response of the DMCI operated with CMS-FDO and CMS-VDO is shown by starting the inverter abruptly at rated voltage. In case of CMS-FDO operated DMCI as shown in Fig. 13(a), the output voltage of the modules jumps from 0 V to the bias voltage, V_{in} as given by (5) for $\omega t = 0$. The startup results in LC excitation between the input inductor and capacitor producing peak input current of 18.6 A. In Fig. 13(b), dynamic response of DMCI operated with CMS-VDO is shown. As the required module output voltages given by (6) is $0.5V_m$ for $\omega t = 0$ which is lower for CMS-VDO operated DMCI compared with CMS-FDO operated DMCI, the LC excitation is lower resulting in peak inductor current is 11.9 A.

Fig. 14 shows the efficiency of the DMCI operated with CMS-FDO and CMS-VDO for various test conditions. Fig. 14(a) provides the results of the DMCI for $g = 1.2$ with varying load. At full load ($R = 30\,\Omega$), the efficiency of the DMCI, operated with CMS-VDO, is found to be 94.77% compared to 91.50% obtained using CMS-FDO. The higher efficiency of the CMS-VDO-based DMCI is due to its lower circulating (reactive) power that yields in reduced conduction, switching, and core losses. For both of the modulation schemes, the diminished efficiency of the DMCI at reduced load is attributed to the constant voltage dependent losses. However, the difference in the efficiencies of the DMCI operated with CMS-FDO and CMS-VDO amplifies further for lower load. Higher drop in the efficiency of the DMCI operated with CMS-FDO are attributed to the higher current ripple of the input and output inductors resulting in a higher magnetic core losses. At low load ($R = 180\,\Omega$), the measured efficiency is 85.03% and 76.11% for DMCI operated with CMS-VDO and CMS-FDO, respectively.

Inverters are typically expected to maintain a constant output voltage with variable input voltage [3], [5], [24]. Hence, the performances of the two modulation schemes for the DMCI are also compared with variable normalized gain (input voltage) for a set output voltage, as captured in Fig. 14(b). The difference in efficiencies of the DMCI operated with CMS-FDO and CMS-VDO at high g (low input voltage) is found to be small due to similar reactive power generation and current stress yielded by the two modulation schemes as discussed in Section III and shown in Fig. 7. In contrast, the efficiencies of the DMCI operated with CMS-FDO and CMS-VDO is found to be higher at low g (high input voltage), as shown in Fig. 14(b).

Fig. 15 provides the estimated loss distribution of the DMCI operated with CMS-FDO and CMS-VDO for various normalized gain which follows the experimental data shown in Fig. 14(b). In case of the CMS-VDO, the total switch loss increases slightly with g due to increase in overall RMS current through the switches. In contrast, the total switch loss for CMS-FDO decreases with g due to significant drop in ripple current as given by (20) resulting in drop in the RMS current through the switches. The magnetic winding and core losses [12] which have high dependency on the ripple current decreases with g for both CMS-FDO and CMS-VDO operated DMCI.

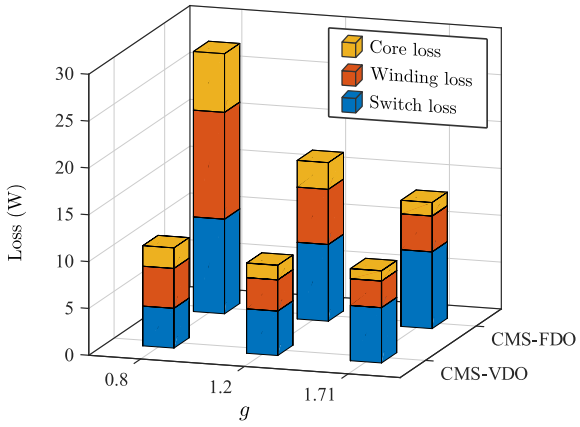

Fig. 15. Comparison of estimated loss CMS-FDO, and CMS-VDO-based DMCI operated with constant $V_o = 85$ V RMS and $R = 30\ \Omega$.

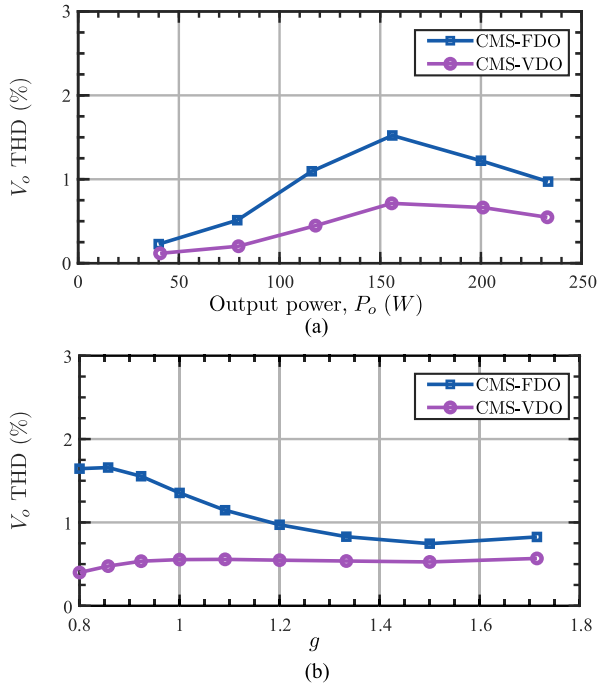

Fig. 16. Comparison of output voltage THD of CMS-FDO, and CMS-VDO based DMCI operated with a constant $V_o = 85$ V RMS against (a) varying output power for $V_{\text{in}} = 100$ V and (b) varying normalized gain with a load of $R = 30\ \Omega$.

In Fig. 15, the winding loss is obtained by considering the skin and proximity effect on the wire while the magnetic core loss is estimated using Steinmetz's equation. The aggregate loss of the DMCI operated with CMS-VDO remains nearly the same even with wide g variation. For the CMS-FDO-based DMCI, the aggregate loss reduces significantly with g (higher input voltage) due to progressively lower reactive-power generation and ripple current.

In Fig. 16, the output-voltage THDs of the DMCI operated with CMS-FDO and CMS-VDO are shown. The THD of the DMCI operated with CMS-FDO and CMS-VDO for wide load variation is shown in Fig. 16(a). It is found that the THD is lower

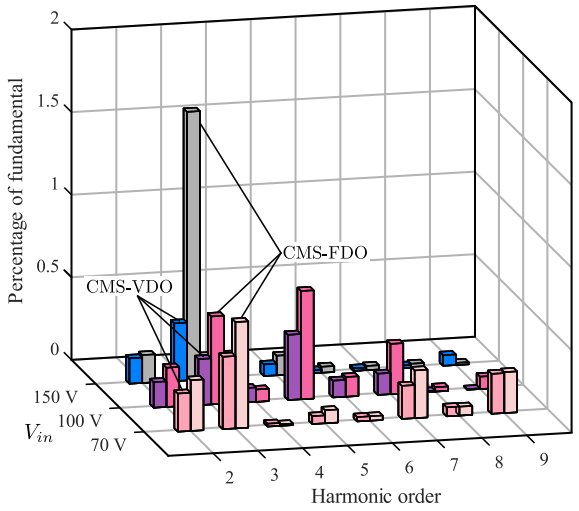

Fig. 17. Harmonic analyses of the output voltage of the CMS-VDO- and CMS-FDO-based DMCI relative to the fundamental harmonic: $V_{in} = 70$ V, 100 V and 150 V, $V_o = 85$ V RMS ($g = 1.2$), and $R = 30\ \Omega$.

than 2% for DMCI operated with CMS-FDO while the THD is lower than 1% for DMCI operated with CMS-VDO. While the trend of THD is similar in both the modulation schemes for varying load, the offset can be accounted by higher ripple current which results in non-linear losses [12]. The THD for varying g is shown in Fig. 16(b) for both the modulation schemes. The THD trend is similar to the ripple current dependency shown in Fig. 8(b).

The output-voltage THD of the DMCI operated with CMS-VDO is found to be lower than that obtained with CMS-FDO as corroborated with Fig. 17. The THD originates in the DMCI due to the nonlinearity and parasitic elements of the inverter resulting in deviation from the ideal relation developed for the module output voltages captured by (5) and (6) for the DMCI operated with CMS-FDO and CMS-VDO, respectively. The major contributors to the output-voltage THD are the 3rd, 5th, and 7th harmonics for both the modulation schemes. In Fig. 17, the odd-harmonic content compared with CMS-VDO modulated DMCI is nearly half of CMS-FDO modulated DMCI resulting in an overall better THD.

V. Conclusion

This article provides a parametric and experimental comparison between CMS-VDO- and CMS-FDO-based single-phase DMCI. Unlike the CMS-FDO, in CMS-VDO, the dc-offset voltage is varied as a function of the inverter peak output voltage for duty-cycle generation of each of the two dc/dc converter modules of the DMCI. Compared to the CMS-FDO-based DMCI, CMS-VDO-based DMCI yields a lower module output voltage, which results in lower voltage stress on the switches and lower input and output inductor-current ripples. CMS-VDO also reduces the reactive (circulating) power flowing between the two modules, which enhances the inverter efficiency over a wide operating range. The analyses described in this article are ratified with experimental validations. For the DMCI hardware prototype,

overall, the CMS-VDO-based DMCI yields higher efficiency, lower switch voltage stress, and lower THD compared to the CMS-FDO-based DMCI.

REFERENCES

[1] S. D'Silva, M. Shadmand, S. Bayhan, and H. Abu-Rub, "Towards grid of microgrids: Seamless transition between grid-connected and islanded modes of operation," *IEEE Open J. Ind. Electron. Soc.*, vol. 1, pp. 66–81, 2020.

[2] S. Gupta, M. F. Umar, M. B. Shadmand, and S. K. Mazumder, "Self-synchronization scheme for network of grid-following and grid-forming photovoltaic inverters," in *Proc. 47th Annu. Conf. IEEE Ind. Electron. Soc.*, 2021, pp. 1–6, doi: 10.1109/IECON48115.2021.9589752.

[3] J. M. A. Myrzik and M. Calais, "String and module integrated inverters for single-phase grid connected photovoltaic systems - A review," in *Proc. IEEE Bologna Power Tech Conf. Proc.*, 2003, vol. 2, pp. 1–8, doi: 10.1109/PTC.2003.1304589.

[4] G. Oriti, A. L. Julian, and N. J. Peck, "Power-electronics-based energy management system with storage," *IEEE Trans. Power Electron.*, vol. 31, no. 1, pp. 452–460, Jan. 2016.

[5] Y. M. Chen, Y. C. Liu, S. C. Hung, and C. S. Cheng, "Multi-input inverter for grid-connected hybrid PV/wind power system," *IEEE Trans. Power Electron.*, vol. 22, no. 3, pp. 1070–1077, May 2007.

[6] Y. Tang, S. Xie, and C. Zhang, "Single-phase Z-source inverter," *IEEE Trans. Power Electron.*, vol. 26, no. 12, pp. 3869–3873, Dec. 2011.

[7] T. N. Gautham, R. Reddivari, and D. Jena, "A cost-effective single-phase semi flipped gamma type magnetically coupled impedance source inverters," *Int. J. Circuit Theory Appl.*, vol. 49, no. 4, pp. 1078–1102, 2021, doi: 10.1002/cta.2865.

[8] D. Cao, S. Jiang, X. Yu, and F. Z. Peng, "Low-cost semi-Z-source inverter for single-phase photovoltaic systems," *IEEE Trans. Power Electron.*, vol. 26, no. 12, pp. 3514–3523, Dec. 2011.

[9] S. Ćuk and R. D. Middlebrook, "Advances in switched-mode power conversion part I," *IEEE Trans. Ind. Electron.*, vol. IE-30, no. 1, pp. 10–19, Feb. 1983.

[10] R. O. Cáceres and I. Barbi, "A boost DC-AC converter: Analysis, design, and experimentation," *IEEE Trans. Power Electron.*, vol. 14, no. 1, pp. 134–141, Jan. 1999.

[11] S. Gupta and S. K. Mazumder, "A differential-mode isolated AC/AC converter," *IEEE Trans. Power Electron.*, vol. 38, no. 10, pp. 12846–12858, Oct. 2023.

[12] M. Mohamadi, S. K. Mazumder, and N. Kumar, "Integrated magnetics design for a three-phase differential-mode rectifier," *IEEE Trans. Power Electron.*, vol. 36, no. 9, pp. 10561–10570, Sep. 2021.

[13] A. A. Aboulnaga and A. Emadi, "Performance evaluation of the isolated bidirectional Ćuk converter with integrated magnetics," in *Proc. IEEE Annu. Power Electron. Specialists Conf.*, 2004, vol. 2, pp. 1557–1562, doi: 10.1109/PESC.2004.1355657.

[14] S. Cuk, "A new zero-ripple switching DC-to-DC converter and integrated magnetics," *IEEE Trans. Magn.*, vol. 19, no. 2, pp. 57–75, Mar. 1983.

[15] D. P. Fernandez, R. A. Fantino, J. C. Balda, and S. K. Mazumder, "Inductor and transformer-coupled magnetic structure for zero-ripple DC-DC Ćuk converter," in *Proc. IEEE Appl. Power Electron. Conf. Expo.*, 2021, pp. 654–659, doi: 10.1109/APEC42165.2021.9487405.

[16] S. Mehrnami and S. K. Mazumder, "Discontinuous modulation scheme for a differential-mode Ćuk inverter," *IEEE Trans. Power Electron.*, vol. 30, no. 3, pp. 1242–1254, Mar. 2015.

[17] S. Gupta and S. K. Mazumder, "A novel modulation scheme for isolated PWM active-clamp Ćuk DC/DC converter," *IEEE Trans. Power Electron.*, vol. 37, no. 12, pp. 14966–14980, Dec. 2022.

[18] F. Barzegar and S. Cuk, "Solid-state drives for induction motors: Early technology to current research," in *Proc. IEEE Region 6 Conf.*, 1982, vol. 6, pp. 15–18.

[19] B. Han, J. S. Lai, and M. Kim, "Bridgeless Cuk-derived single power conversion inverter with reactive-power capability," *IEEE Trans. Power Electron.*, vol. 35, no. 3, pp. 2629–2645, Mar. 2020.

[20] C. Bao, S. Gupta, and S. K. Mazumder, "Modeling and analysis of peak-current-controlled differential mode Ćuk inverter," in *Proc. IEEE 12th Int. Symp. Power Electron. Distrib. Gener. Syst.*, 2021, pp. 1–7, doi: 10.1109/PEDG51384.2021.9494167.

[21] K. Tank, M. M. Garg, and S. K. Mazumder, "A New continuous modulation scheme for differential mode boost inverter," in *Proc. IEEE 13th Int. Symp. Power Electron. Distrib. Gener. Syst.*, 2022, pp. 1–6, doi: 10.1109/PEDG54999.2022.9923272.

[22] R. W. Erickson and D. Maksimović, *Fundamentals of Power Electronics*, 2nd Ed., Springer New York, NY, 2007, doi: 10.1007/B100747.

[23] J. Mühlethaler, J. Biela, J. W. Kolar, and A. Ecklebe, "Core losses under DC bias condition based on Steinmetz parameters," in *Proc. Int. Power Electron. Conf.–ECCE Asia*, 2010, pp. 2430–2437, doi: 10.1109/IPEC.2010.5542385.

[24] M. G. Varzaneh, A. Rajaei, M. Forouzesh, Y. P. Siwakoti, and F. Blaabjerg, "A single-stage multi-port buck-boost inverter," *IEEE Trans. Power Electron.*, vol. 36, no. 7, pp. 7769–7782, Jul. 2021.

Kartik Tank received the B.Tech. degree in electrical engineering from Rajasthan Technical University, Kota, India, in 2020, and the M.Tech. degree in power electronics and drives specialization from the Department of Electrical Engineering, Malaviya National Institute of Technology Jaipur, India, in 2022.

His current research interests include modeling and control of dc–dc converters, differential mode inverters, and electric vehicle chargers.

Shantanu Gupta (Graduate Student Member, IEEE) received the B.Tech. degree in electrical engineering from Delhi Technological University, New Delhi, India, in 2016. He is currently working toward the Ph.D. degree in electrical and computer engineering in the University of Illinois Chicago, Chicago, IL, USA.

From 2016 to 2019, he was a Research Engineer with TEX E.G., Japan. His work involved working on embedded and power electronics systems. Among the projects he worked on were the development of a semiconductor wafer alignment machine and a motor driver for a refrigerator compressor. His research interests include soft-switching techniques and power electronics topologies.

Mr. Gupta serves as a Reviewer for IEEE TRANSACTIONS ON POWER ELECTRONICS and IEEE TRANSACTIONS ON INDUSTRIAL ELECTRONICS.

Man Mohan Garg (Senior Member) received the B.E. degree in electrical engineering from the M.B.M. University Jodhpur, Jodhpur, India, in 2008, and the M.Tech. and Ph.D. degrees in electrical engineering from the Indian Institute of Technology (IIT) Roorkee, Roorkee, India, in 2010 and 2016, respectively.

He is currently serving with the Department of Electrical Engineering, Malaviya National Institute of Technology (MNIT) Jaipur, India, as an Assistant Professor. Prior to joining MNIT Jaipur in June 2020, he has worked as an Assistant Professor with the Department of Electrical Engineering, National Institute of Technology (NIT) Rourkela, India. He completed his Postdoctoral with the Department of Electrical Engineering, IIT Kanpur, India. His current research interests include design, modeling, and control of power electronic converters, grid integration of distributed renewable energy sources, dc microgrid, electric vehicles, cyber-physical energy systems, and LED driver circuits. His research work has been published in IEEE TRANSACTIONS/JOURNALS and other reputed international journals, book chapters and conferences.

Dr. Garg is an active editorial board member in several reputed journals and conferences.

Sudip K. Mazumder (Fellow, IEEE) received the Ph.D. degree in electrical and computer engineering from Virginia Tech, Blacksburg, VA, USA, in 2001.

He has been the President of NextWatt LLC, Westbury, IL, USA, since 2008 and a Professor with the University of Illinois Chicago (UIC), Chicago, IL, USA, since 2001. He has over 30 years of professional experience and has held research and development and design positions in leading industrial organizations and has served as a technical consultant for several industries.

Dr. Mazumder was chosen as a recipient of the honorary title of UIC Distinguished Professor to be effective in AY'23 pending Board of Trustees approval, in June 2023. He was named a Fellow of the American Association for the Advancement of Science (AAAS), in 2020, a Fellow of the Institute of Electrical and Electronics Engineers (IEEE), in 2016, and a Fellow of the Asia-Pacific Artificial Intelligence Association (AAIA) in 2022. He serves as the Editor in Large for IEEE Transactions on Power Electronics (TPEL) since 2019 and served as an IEEE Distinguished Lecturer between 2016 and 2019. He has been serving as an Administrative Committee Member for IEEE PELS, since 2015. He has also been serving as a Member-at-Large for IEEE PELS, since 2020. He had served as the Chair for the IEEE PELS Technical Committee on Sustainable Energy Systems, from 2015 to 2020. He serves as the General Chair for IEEE PEDG Conference in 2023. He is the recipient of the 2023 IEEE Power & Energy Society's Ramakumar Family Renewable Energy Excellence Award, and several IEEE awards/honors, including IEEE Transactions on Power Electronics Prize Paper Awards (2022, 2002) and Highlighted Papers (2023, 2022, 2018), Featured Article for IEEE Transactions on Biomedical Engineering (2023), IEEE Conference Best Paper Award (2013), and IEEE International Future Energy Challenge Award (2005).

Moien Mohamadi (Student Member, IEEE) received the Ph.D. degree from the University of Illinois at Chicago, Chicago, IL, USA, in 2022.

He worked with the Laboratory for Energy and Switching-Electronics Systems (LESES) to improve efficiency and power density of off-board chargers. He is currently working with Tesla, Austin, TX, USA. He has been working in power electronics research and development since 2014. His research interests include optimal design and hardware realization of highly efficient and compact power electronics converter, high-frequency magnetic design, optimization, and hardware realization, and soft-switching power electronics.

Dr. Mohamadi is a member of PES community.